




# Cell-membrane targeting sonodynamic therapy combination with FSP1 inhibition for ferroptosis-boosted immunotherapy

Jian Chen<sup>a,1</sup>, Qiyu Zhan<sup>a,1</sup>, Lie Li<sup>a</sup>, Simin Xi<sup>a</sup>, Longmei Cai<sup>c,\*</sup>, Ruiyuan Liu<sup>a,\*\*</sup> , Lujia Chen<sup>b,\*\*\*</sup>

<sup>a</sup> Biomaterials Research Center, School of Biomedical Engineering, Southern Medical University, Guangzhou, 510515, PR China

<sup>b</sup> Breast Center, Department of General Surgery, Nanfang Hospital, Southern Medical University, Guangzhou, 510515, PR China

<sup>c</sup> Department of Radiation Oncology, Nanfang Hospital, Southern Medical University, Guangzhou, 510515, PR China

## ARTICLE INFO

### Keywords:

Cell membrane targeting  
Sonodynamic therapy  
ferroptosis  
FSP1 inhibition  
Immunogenic cell death

## ABSTRACT

Cell membrane targeting sonodynamic therapy could induce the accumulation of lipid peroxidation (LPO), drive ferroptosis, and further enhances immunogenic cell death (ICD) effects. However, ferroptosis is restrained by the ferroptosis suppressor protein 1 (FSP1) at the plasma membrane, which can catalyze the regeneration of ubiquinone (CoQ10) by using NAD(P)H to suppress the LPO accumulation. This work describes the construction of US-active nanoparticles (TiF NPs), which combine cell-membrane targeting sonosensitizer TBT-CQI with FSP1 inhibitor (iFSP1), facilitating cell-membrane targeting sonodynamic-triggered ferroptosis. TiF NPs could induce a sonodynamic effect, which promotes lipid peroxidation and drives apoptosis. Furthermore, TiF NPs could suppress FSP1, induce CoQ10 depletion, down-regulate the NADH, enhance LPO accumulation, and finally induce ferroptosis. *In vitro* results demonstrated that synergetic cell membrane targeting SDT/FSP1 inhibition triggered immunogenic cell death (ICD). Moreover, the as-synthesized TiF NPs-mediated cell membrane targeting SDT/FSP1 inhibition thoroughly inhibited the tumor growth and simultaneously activated antitumor immunity to suppress lung metastasis. This work represents a promising tumor therapeutic strategy combining cell membrane targeting SDT and FSP1 inhibition, potentially inspiring further research in developing logical and effective cancer therapies based on synergistic SDT/ferroptosis.

## 1. Introduction

Sonodynamic therapy (SDT) has received a lot of interest recently for treating tumors, due to its deep penetration, noninvasiveness, high therapeutic efficiency, and low side effects [1–6]. SDT activates sonosensitizers through ultrasound (US), generating cytotoxic reactive oxygen species (ROS) that induce oxidative stress and tumor cell death [7–9]. Moreover, the penetration depth (>10 cm), spatiotemporal resolution, controllability, and safety of ultrasonic irradiation are greatly superior [10,11]. Additionally, it has been demonstrated that SDT induces immunogenic cell death (ICD), which can activate a potent anti-tumor immune response [12–17]. Up to now, various organic molecules or nanoparticles with sonodynamic activity have been widely exploited for tumor SDT via disturbing intracellular redox equilibrium and

triggering an immune response [18–23]. Although encouraging, the actual performance is significantly hampered by the reactive oxygen species (ROS) severely constrained lifespan and transport distance, and as a result, the resulting ICD is surprisingly constrained. As known, oxidative stress resulting from the accumulation of ROS in the cell membrane can result in lipid peroxidation (LPO), which alters the physiological functions of cell membranes by disrupting membrane permeability and destroying membrane integrity [24–27]. Moreover, LPO could destroy the cell membrane integrity and trigger the release of DMAP, which could strongly induce immunogenic cell death (ICD) for activating antitumor immunity. In this regard, accumulating sonosensitizers in cell membrane appears to be a potential approach for the enhancement of anticancer SDT based on LPO amplification and ICD triggering.

\* Corresponding author.

\*\* Corresponding author.

\*\*\* Corresponding author.

E-mail addresses: [clm520@i.smu.edu.cn](mailto:clm520@i.smu.edu.cn) (L. Cai), [ruiyliu@smu.edu.cn](mailto:ruiyliu@smu.edu.cn) (R. Liu), [dr\\_chenlj@smu.edu.cn](mailto:dr_chenlj@smu.edu.cn) (L. Chen).

<sup>1</sup> Both authors contributed equally to this work.

To date, some organic photosensitizers can function as sonosensitizers to treat tumor, including chlorin e6, IR780, porphyrin, 5-aminolevulinic acid, phthalocyanines, xanthenes, rose Bengal, and indocyanine green (ICG), and so on [28–31]. Besides, some inorganic nanoparticles can generate ROS under US irradiation, such as TiO<sub>2</sub> nanoparticles (NPs), MnWO<sub>x</sub>, PtCu<sub>3</sub>, silicon NPs, quantum dots (QDs), black titanium NPs, and black phosphorus-based materials [32–35]. Those sonosensitizers give more potentialities for the development of sonodynamic therapy. However, some drawbacks of those sonosensitizers cannot be ignored. For instance, organic materials such as Ce6 suffer from phototoxicity, low water solubility, and deficiency of targeting ability. Moreover, the low metabolism and low biodegradability of inorganic material will limit their biomedical applications. However, to date, cell membrane-targeting sonosensitizers have seldom been reported.

Ferroptosis is a newly discovered form of programmed cell death, which is induced by unrestricted lipid peroxidation and subsequent cell membrane rupture [36–40]. In contrast to other regulated cell death pathways including apoptosis and necrosis, cancer cells could be particularly vulnerable to ferroptosis. Nevertheless, the development of ferroptosis-based anticancer therapies is constrained by the ferroptosis regulatory networks in the tumor. Recent findings on ferroptosis regulation mechanisms suggest that ferroptosis is blocked by the CoQ oxidoreductase ferroptosis suppressor protein 1 (FSP1) at the plasma membrane, which can catalyze the recycling of coenzyme Q10 (CoQ10) to ubiquinol (CoQ10H2) to detoxify LPO [41–43]. Therefore, ferroptosis can be triggered by inhibition of FSP1, which down-regulates the activity of FSP1, decreases the NADH, suppresses the CoQ10, elevates the level of LPO in tumor cells, and finally induces ferroptosis [44–46]. Hence, the combination of FSP1 inhibition with enhanced LPO accumulation could trigger ferroptosis and improve tumor immunotherapy.

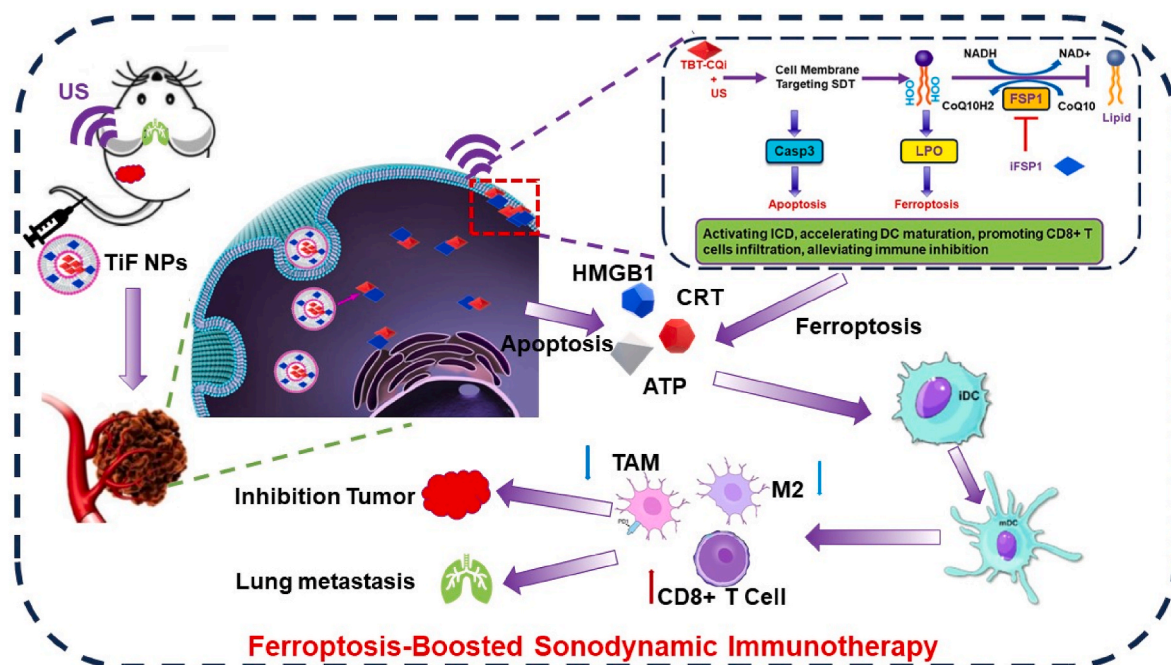
It is hypothesized that the synergistic combination of cell membrane-targeting sonosensitizers and FSP1 inhibitor could offer an optimal way to enhance LPO generation and suppress the trap of LPO for triggering ferroptosis, inducing ICD, and provoking antitumor immunity. In this work, we designed multifunctional nanoparticles (TiF NPs) for cell-membrane targeting SDT and FSP1 inhibition synthesized therapy of tumor (Scheme 1). Typically, a D-A- $\pi$ -A1 structure cell membrane-targeting sonosensitizer (TBT-CQi) and FSP1 inhibitor (iFSP1) were encapsulated in DSPE-PEG2000 using thin-film hydration method. After

the uptake of the TiF NPs by 4T1 cells, the TBT-CQi in the nanoparticles can accumulate in the cell membrane and generate ROS under US irradiation, which damages cell membrane, improves the LPO level, and induces apoptosis. Alternatively to the cell membrane targeting SDT of TBT-CQi, the iFSP1 in the nanoparticles can suppress FSP1 expression, increase NADP<sup>+</sup>/NADPH ratio, decrease CoQ10, further suppress the detoxification capability of the FSP1-mediated lipid peroxide reducing system to drive ferroptosis. Meanwhile, cell membrane-targeting SDT plus FSP1 inhibition based on TiF NPs can activate impressive ICD with the release of DAMPs and increase the effectiveness of immunotherapy. This study exhibited the promising potential of cell membrane-targeting SDT combination with FSP1 inhibition for ferroptosis-boosted sonodynamic immunotherapy, which provides an avenue for therapeutic intervention in the clinic.

## 2. Experimental methods

### 2.1. Synthesis of TBT-CQi

TBT-CQ (639 mg, 1 mmol) and iodoethane (232.5 mg, 1.5 mmol) were added into CH<sub>3</sub>CN (10 mL). The reaction was refluxed overnight under N<sub>2</sub> protection. The solution was evaporated. The solvent was evaporated in a vacuum. The resulting mixture was filtered off, washed with cold ether, and dried over in a vacuum drier. The obtained residue was purified by gel column chromatography with dichloromethane/methanol (from 50:1 to 20:1) as eluent, giving to desired product as black solid (407 mg), yield 52%. <sup>1</sup>H NMR (600 MHz, CDCl<sub>3</sub>)  $\delta$  8.85–8.87 (d,  $J$  = 8.6Hz, 1H), 8.27–8.35 (m, 5H) 8.17–8.18 (d,  $J$  = 7.5Hz, 1H), 8.09–8.12 (t, 1H), 8.05–8.06 (d,  $J$  = 4.2Hz, 1H), 7.94–7.95 (d,  $J$  = 8.5Hz, 2H), 7.80–7.82 (d,  $J$  = 7.5Hz, 1H), 7.46 (s, 2H), 7.33–7.35 (t, 5H), 7.22–7.25 (t, 4H), 7.11–7.22 (t, 4H), 3.76–3.77 (d,  $J$  = 9.8Hz, 2H), 1.45–1.48 (t, 3H). <sup>13</sup>C NMR (300 MHz, CDCl<sub>3</sub>) 154.65, 152.85, 150.83, 148.99, 148.95, 147.88, 146.87, 141.02, 137.26, 136.15, 134.98, 130.76, 130.45, 130.21, 129.73, 128.76, 127.29, 126.94, 126.65, 126.02, 124.99, 124.66, 124.47, 123.76, 122.83, 121.63, 121.13, 112.36, 103.38, 51.10, 20.01. ESI-HRMS  $m/z$ : calcd. for C<sub>42</sub>H<sub>30</sub>N<sub>5</sub>S<sub>2</sub> [M – I]<sup>+</sup> 668.1937, found: 654. 668.1943.



**Scheme 1.** The Schematic illustration of multifunctional nanoparticles for ferroptosis-boosted sonodynamic therapy and suppressing FSP1/CoQ10 pathways.

## 2.2. Preparation of TiF NPs

TiF NPs were prepared by a well-established thin-film hydration method. TBT-CQi (1 mg), iFSP1 (0.8 mg) and DSPE-PEG2000 (4 mg) were respectively dissolved into 5 mL of  $\text{CHCl}_3$  and mixed homogeneously. The organic solvent was removed, then the double distilled water was drop added under ultrasonic conditions, then transferred to a dialysis bag (molecular weight cutoff (MWCO) = 3000) and dialyzed against deionized water for 24 h. The concentration of TBT-CQi and iFSP1 in TiF NPs was determined by the Standard curve method. TBT-CQi was encapsulated by DSPE-PEG2000 to obtain TB NPs for control experiments.

## 2.3. The detection of ROS generated from TiF NPs by SDT via DCFH

2',7'-Dichlorodihydrofluorescein (DCFH), which was obtained from 2',7'-dichlorodihydrofluorescein diacetate (DCFH-DA), was used as the probe to evaluate ROS generation. Add TiF NPs solution with a stock concentration (TBT-CQi 1 mM) to the aqueous solution containing 10  $\mu\text{M}$  DCFH, and the final TBT-CQi concentration is 5  $\mu\text{M}$ . The above solution is treated the cells with US irradiation (1.0 MHz, 1.5  $\text{W}/\text{cm}^2$ , 50 % duty cycle) for different periods of time. The change in the fluorescence signal of the indicator is monitored by a fluorescence spectrometer. The excitation wavelength is 480 nm, and the fluorescence intensity of DCFH at 525 nm is recorded to indicate ROS generation. A curve was drawn to compare the fluorescence changes of DCFH in different solutions, so as to obtain the difference in ROS generation capacity.

## 2.4. The detection of ROS generated from TiF NPs by SDT via DPBF

1,3-diphenylisobenzofuran (DPBF) was used as the probe to evaluate ROS generation. Add TiF NPs solution with a stock concentration (TBT-CQi 1 mM) to the aqueous solution containing 50  $\mu\text{M}$  DPBF, and the final TBT-CQi concentration is 5  $\mu\text{M}$ . The above solution is treated the cells with US irradiation (1.0 MHz, 1.5  $\text{W}/\text{cm}^2$ , 50 % duty cycle) for different periods of time. The change in the absorption signal of the indicator is monitored by a UV-vis spectrometer.

## 2.5. ROS generated from SDT detection with electron paramagnetic resonance (EPR)

TEMPO was used as the trapping agent for  $^1\text{O}_2$ . TEMPO was dissolved in  $\text{CH}_3\text{OH}$ , which was further added into TiF NPs aqueous solution to reach a final concentration of 10  $\mu\text{M}$  and 50  $\mu\text{M}$  for TBT-CQi and trapping agent, respectively. The EPR spectra of the mixtures were recorded before and after US irradiation (1.0 MHz, 1.5  $\text{W}/\text{cm}^2$ , 50 % duty cycle, 10min). The electron paramagnetic resonance (EPR, Bruker A300) spectra were measured to evaluate ROS generation.

## 2.6. Intracellular lipid peroxidation (LPO) generation

4T1 cells were seeded in 96-well plates and pre-cultured for 24 h, and then the medium was replaced by TiF NPs solution (TBT-CQi concentration: 10  $\mu\text{M}$ , iFSP1 concentration: 20  $\mu\text{M}$ ) for 4 h, and then washed with phosphate buffer saline (PBS). The media were replaced by serum-free media containing BODIPY<sup>TM</sup> 581/591C11 (5  $\mu\text{M}$ ) after administration for 24 h and incubated for 20 min. Similarly, the cells were treated the cells with US irradiation (1.0 MHz, 1.5  $\text{W}/\text{cm}^2$ , 50 % duty cycle, 10 min). Then, the cells were washed with PBS and treated with 4 % paraformaldehyde, followed by staining with DAPI for CLSM observation.

## 2.7. Cellular adenosine triphosphate (ATP) detection

4T1 cells were seeded in 6-well plates ( $2 \times 10^5$  cells/well) for 12 h. After that, the cells were treated with TiF NPs (TBT-CQi concentration:

10  $\mu\text{M}$ , iFSP1 concentration: 20  $\mu\text{M}$ ) for 4 h. Then, the cells were treated with US irradiation (1.0 MHz, 1.5  $\text{W}/\text{cm}^2$ , 50 % duty cycle, 10min). After further incubation for 24 h, the cells were collected to detect the intracellular ATP concentrations by the ATP assay Kit, and the results were normalized by protein concentrations measured by BCA.

## 2.8. Intracellular CoQ10 and MDA assay

4T1 cells were seeded in 6-well plates ( $2 \times 10^5$  cells/well) for 12 h. After that, the cells were treated with TiF NPs (TBT-CQi concentration: 10  $\mu\text{M}$ , iFSP1 concentration: 20  $\mu\text{M}$ ) for 4 h. The cells were treated with US irradiation (1.0 MHz, 1.5  $\text{W}/\text{cm}^2$ , 50 % duty cycle, 10min). The CoQ10 amount was detected using CoQ10 assay kit; the MDA amount was monitored using MDA assay kit.

## 2.9. Intracellular NADH and NAD<sup>+</sup> assay

4T1 cells were seeded in 6-well plates ( $2 \times 10^5$  cells/well) for 12 h. After that, the cells were treated with TiF NPs (TBT-CQi concentration: 10  $\mu\text{M}$ , iFSP1 concentration: 20  $\mu\text{M}$ ) for 4 h. The cells were treated with US irradiation (1.0 MHz, 1.5  $\text{W}/\text{cm}^2$ , 50 % duty cycle, 10min). The NADH amount and NAD<sup>+</sup>/NADH were detected using NAD<sup>+</sup>/NADH assay kit.

## 2.10. Construction of tumor models

Five or six-week-old female BALB/c mice were provided by the Animal Center of Southern Medical University. All animal experiments were carried out under the guidance of the protocols approved by the local Ethical Committee in compliance with the Chinese law on experimental animals and followed the regulations of the Institutional Animal Care and Use Committee of South Medical University (SCXK 2021-0041). All mice were kept in SPF-level feeding conditions with adequate water and food. The temperature is kept at 26 °C, the humidity is 50 %, and a 12 h light/dark cycle.

Female mice (BALB/c, 6–8 weeks old) were inoculated subcutaneously with mouse breast cancer cells. 100  $\mu\text{L}$  4T1 cells ( $2 \times 10^6$ ) suspensions were injected subcutaneously into the right limb of the mice. Three days later, 100  $\mu\text{L}$  4T1 cells ( $2 \times 10^5$ ) suspensions were intravenously injected into mice to obtain a breast cancer model with lung metastases. When tumors reached an average volume of 100  $\text{mm}^3$ , mice were used for *in vivo* imaging and anti-tumor evaluation.

## 2.11. In vivo antitumor activity

The 4T1 tumor-bearing mice were randomly divided into five groups and performed with the following different treatments: group i, PBS injection; group ii, TB NPs injection; group iii, only TiF NPs injection; group iv, TB NPs injection and US irradiation; group v, TiF NPs injection and US irradiation.

Each group contained five mice, and 100  $\mu\text{L}$  of TiF NPs (TBT-CQi concentration: 50  $\mu\text{M}$ , iFSP1 concentration: 100  $\mu\text{M}$ ) were intravenously injected. The US irradiation was performed 24 h after the injection. The US irradiation was carried out with power in the indicated treatment groups (1.0 MHz, 2.0  $\text{W}/\text{cm}^2$ , 50 % duty cycle, 10 min). 24 h after different treatments, one mouse in each group was sacrificed by cervical dislocation for necropsy, and its tumor was collected for tissue slicing and staining. For the left mice, their body weights and tumor sizes were measured every 2 days for a period of 14 days, and the tumor volumes were calculated using the following formula: Volume = (Length  $\times$  Width<sup>2</sup>)/2. At day 3, one mouse of each group was executed and their tumors were collected for hematoxylin and eosin (H&E) staining and TUNEL staining. At day 14, one mouse of each group was executed and their main organs were collected for hematoxylin and eosin (H&E) staining to evaluate the biosafety.

## 2.12. Statistical analysis

Data between two groups were analyzed by an independent *t*-test, and more than two groups were tested by one-way ANOVA followed by a suitable post-hoc analysis. For all tests,  $P < 0.05$  was considered statistically significant. Data were expressed as the mean  $\pm$  SD (standard deviation). All data were analyzed using GraphPad Prism 8.0 software.

## 3. Result and discussion

### 3.1. Preparation and Characterization of TiF NPs

The targeted D-A- $\pi$ -A1 structured organic sonosensitizer, TBT-CQi, was prepared according to the reported methods, and the synthetic details were provided in the Supporting Information (Scheme S1). TBT-CQi and FSP1 inhibitor (iFSP1) were encapsulated into DSPE-PEG2000 by thin-film hydration methods to improve the hydrophilicity and biocompatibility (Fig. 1A). The obtained nanoparticles displayed a spherical morphology with a hydrodynamic size of 157 nm (TB NPs), and 185 nm (TiF NPs), respectively (Fig. 1B and Fig. S6). The size distribution and zeta potentials of the TB NPs and TiF NPs were then exploited by dynamic light scattering (DLS) examination (Fig. 1C and Fig. S7). The surface charge of TiF NPs was confirmed by the Zeta potential analysis. Owing to the positive charge of TBT-CQi (11.21 mV), the surface potential of lipid nanoparticles increased from  $-14$  mV from DSPE-PEG2000 to 5.51 mV from TiF NPs (Fig. 1D). The change in the zeta potential provided more proof that TiF NPs were formatted. Moreover, TiF NPs could be well dispersed and stored in PBS without any aggregation up to 21 days (Figs. S8 and S9).

UV-vis spectrum and fluorescence spectrum of TiF NPs were further monitored. In the UV-Vis spectra of TiF NPs, the peak of iFSP1 at 380 nm and the peak of TBT-CQi at 500 nm were observed in the spectrum of TiF NPs (Fig. 1E). As shown in Fig. S10, TiF NPs emitted NIR fluorescence with an emission peak around 635 nm and a shoulder peak about 685 nm, attributing to TBT-CQi, and peak at 475 nm for iFSP1, respectively. All these results verified the successful fabrication of TiF NPs. Moreover,

the TBT-CQi loadings were  $5.43 \pm 0.47$  % (w/w) in TiF NPs, while the iFSP1 loading was  $4.41 \pm 0.31$  % (w/w) in TiF NPs, according to the UV-Vis analysis (Figs. S11 and S12). Furthermore, absorption and fluorescence spectroscopy were utilized to explore the stability of TiF NPs. As depicted in Figs. S13 and S14, TiF NPs exhibited excellent photostability after US irradiation.

### 3.2. ROS generation Properties under US irradiation

The ROS production of TiF NPs upon sonication irradiation was assessed using 2',7'-dichlorofluorescein (DCFH) as the probe. As shown in Fig. 2A, TiF NPs could produce ROS efficiently upon sonication (1.0 MHz, 50 % duty cycle, 1.5 W/cm<sup>2</sup>). The fluorescent intensity of DCFH with TiF NPs at 522 nm increased under US irradiation, confirming the successful ROS production (Fig. 2B). Furthermore, using 1,3-diphenylbenzofuran (DPBF) as a probe, UV-vis spectroscopy was used to examine the <sup>1</sup>O<sub>2</sub> production capability of TiF NPs under US irradiation (Fig. 2C). The absorption intensities of DPBF declined rapidly, verifying the efficient production of <sup>1</sup>O<sub>2</sub> under US irradiation. However, after treatment with TiF NPs alone, there was barely any change in the absorbance of DPBF (Fig. S15). Additionally, electron spin resonance (ESR) spectroscopy was employed to validate the generation of <sup>1</sup>O<sub>2</sub> (Fig. 1D). The ESR results exhibited a strong characteristic 1:1:1 triple peak of <sup>1</sup>O<sub>2</sub> in the TiF NPs + US group, demonstrating that TiF NPs produced <sup>1</sup>O<sub>2</sub> effectively when exposed to US radiation. All these results confirmed that TiF NPs can be used as an effective sonosensitizer to produce <sup>1</sup>O<sub>2</sub>.

### 3.3. Cellular uptake and sonodynamic effect of TiF NPs In vitro

The cellular uptake of TiF NPs in 4T1 cells was investigated. The red fluorescence from TiF NPs in 4T1 cells was observed under confocal laser scan microscopy (CLSM) and the red fluorescence intensity increased with the extended incubation duration (Fig. S16). Moreover, it seems that TiF NPs mainly accumulated in the cytoplasm and cell membrane, according to real-time fluorescent imaging. The

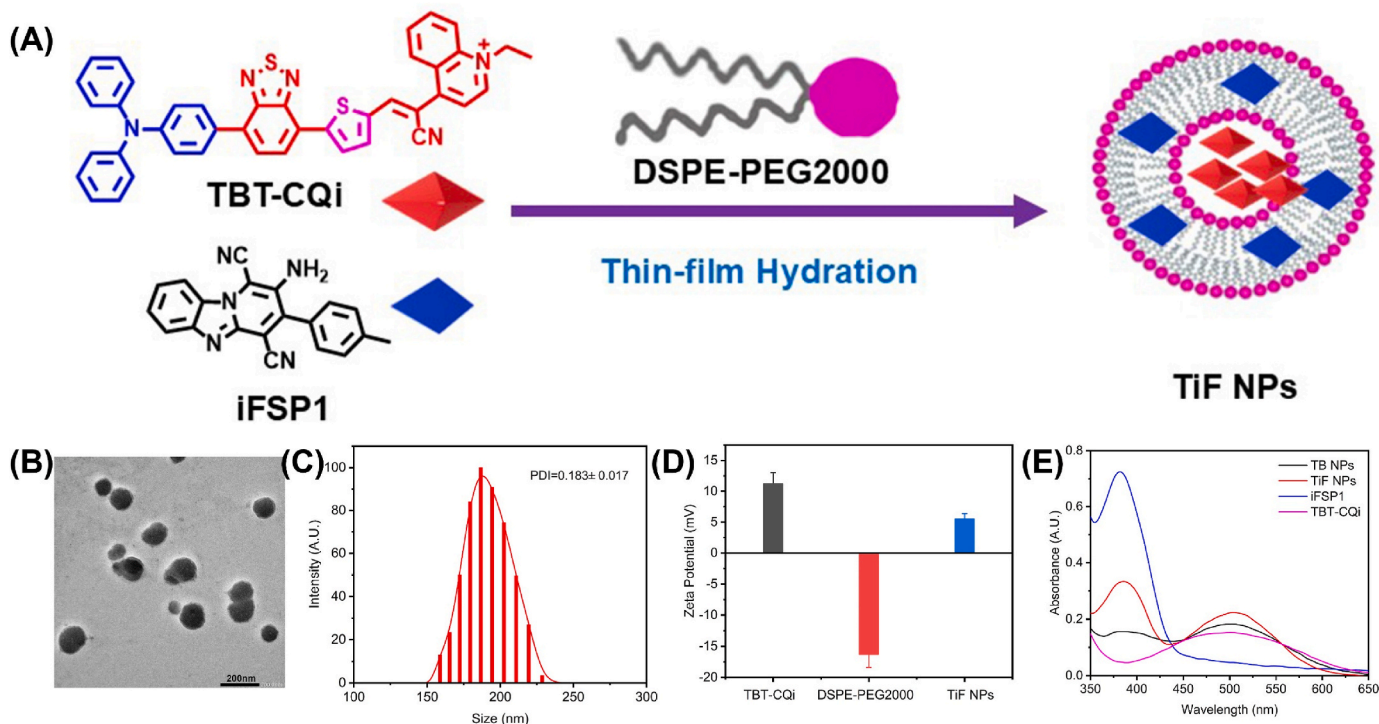


**Fig. 1.** Preparation and characteristics of TiF NPs. (A) The scheme description of TiF NPs. (B) The TEM of TiF NPs, scale bar = 200  $\mu$ m. (C) The DLS of TiF NPs. (D) The zeta potential of TBT-CQi, DSPE-PEG2000, and TiF NPs. (E) The UV-vis absorption spectra of TBT-CQi, TB NPs, iFSP1, and TiF NPs.

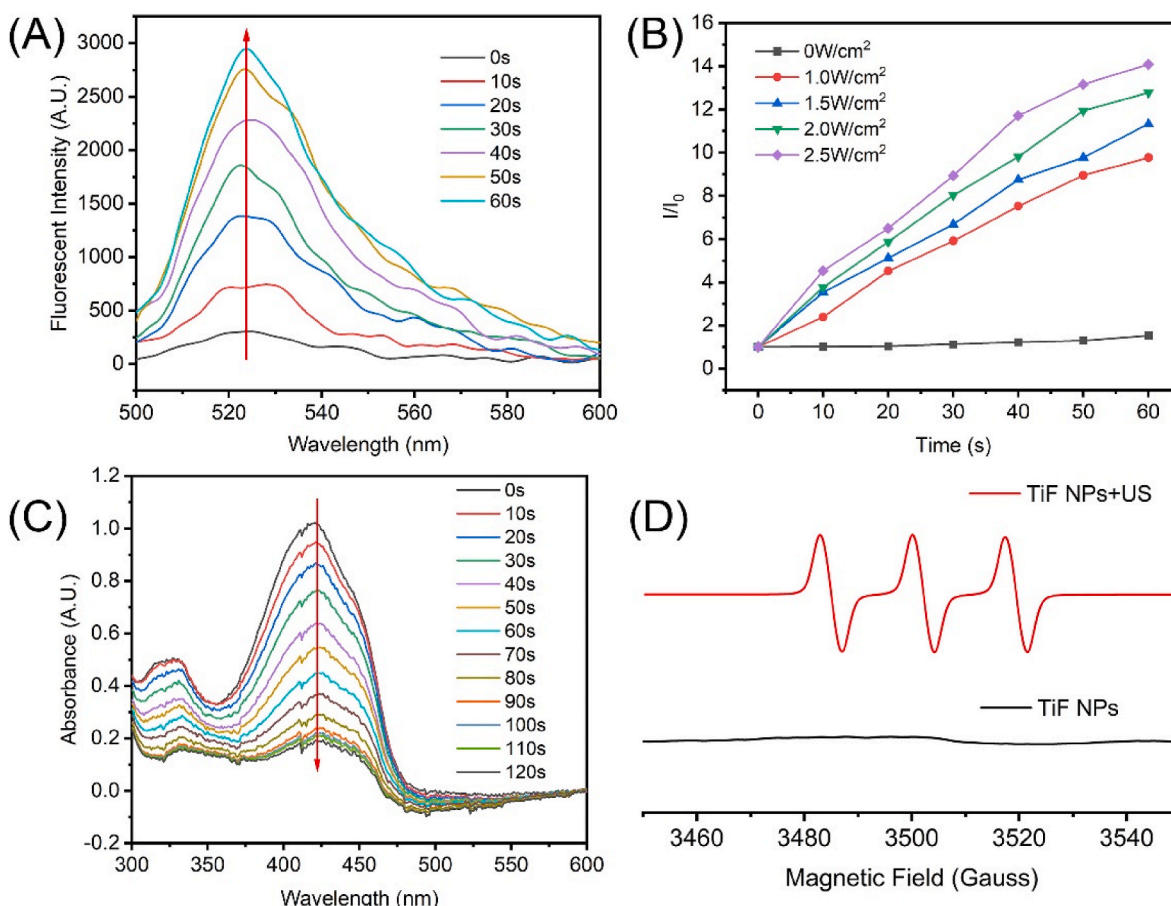


**Fig. 2.** (A) DCFH probe sensing ROS generation in the presence of TiF NPs ([TBT-CQi] = 5  $\mu$ M) in water within 60s ultrasound irradiation (1 MHz, 50 % duty cycle, 1.5 W/cm<sup>2</sup>). (B) Relative fluorescence changes of the DCFH solution at 522 nm under ultrasound irradiation (1.0 MHz, 50 % duty cycle) with different power densities. (C) DPBF probe sensing  $^1O_2$  generation in the presence of TiF NPs ([TBT-CQi] = 5  $\mu$ M) in water within 120s ultrasound irradiation (1.0 MHz, 50 % duty cycle, 1.5 W/cm<sup>2</sup>). (D) ESR spectra demonstrating  $^1O_2$  generation under ultrasound irradiation (1.0 MHz, 50 % duty cycle, 1.5 W/cm<sup>2</sup>), using 2,2,6,6-tetramethylpiperidine (TEMPO) as a spin trapper.

colocalization experiments of TiF NPs with DiO were carried out to examine the cell membrane targeting property of TiF NPs in 4T1 cells. As shown in CLSM images (Fig. 3A), the red fluorescence of TBT-CQi from TiF NPs overlapped well with the green fluorescence from DiO post-co-cubation, manifesting the accumulation of TiF NPs in the cell membrane.

2'-7'-dichlorofluorescein (DCFH) fluorogenic probe was used for ROS detection at the cellular level to verify the TiF NPs' effective ROS generation. DCFH can be oxidized by ROS to produce the extremely fluorescent molecules 2'-7'-dichlorofluorescein (DCF). When applying US irradiation, a certain level of ROS generation was triggered by TB NPs, attributed to its intrinsic sonosensitizer property (Fig. 3B). In comparison, TiF NPs contributed to enhanced ROS production, as evidenced by the more intense green fluorescence, owing to the efficient ROS generation and inhibition of FSP1. Moreover, weak green fluorescence was detected in the cells treated with TB NPs or TiF NPs without US activation. Furthermore, SOSG were selective probes for  $^1O_2$ . Due to the  $^1O_2$  production capacity of TBT-CQi, green fluorescence was observed in the TB NPs + US irradiation group. In contrast, the cells in TiF NPs + US irradiation group showed intense green fluorescence due to effective  $^1O_2$  production and suppression of FSP1 (Fig. 3C and Fig. S17). Notably, no ROS species were detected without US irradiation, confirming that the sonodynamic process of TiF NPs.

Negligible biocompatibility of sonosensitizers is always the primary prerequisite for their biomedical applications. Thus, the cytotoxicity of TiF NPs to tumor 4T1 cells and normal L929 cells was assessed. First, the effect of TiF NPs on 4T1 cell proliferation under US irradiation was

investigated. In addition, to verify the sonosensitization effect, TB NPs were also included. As shown in Fig. 3D and Fig. S18, the TiF NPs and TB NPs exhibited a little cell-toxicity effect in 4T1 cells or L929 cells. For example, the cell survival rates above 80 % at a TiF NPs concentration as high as 10  $\mu$ M, proving TiF NPs to be sufficiently biocompatible for use in medicine. The sonosensitization effect TiF NPs in 4T1 cells was investigated. As displayed in Fig. 3E, the death rate showed a stronger concentration-dependent manner of TiF NPs in the presence of US irradiation. Moreover, the IC<sub>50</sub> of TB NPs was 9.50  $\mu$ M, which was slightly higher than that of TiF NPs under US irradiation (Fig. S19).

#### 3.4. *In vitro* cell-membrane targeting SDT and ferroptosis and immunogenic cell death (ICD) induction

Ferroptosis is a form of cell death due to the accumulation of lipid peroxidation (LPO) in cells [47–49]. Inspired by the cell-membrane targeted property and SDT of TiF NPs, we wonder about the SDT combined with inhibitions of FSP1 to induce ferroptosis and ICD. The LPO level was then detected by CSLM using an LPO sensor (BODIPYTM 581/591C11) (Fig. 4A). As indicated, FSP1 inhibitor treatment could induce a certain degree of LPO, and a stronger green fluorescence was displayed in the PDT group, suggesting greater LPO generation. The significant increase in LPO after TiF NPs + US treatment was confirmed by its stronger green fluorescence than SDT. The intracellular MDA which is a marker of LPO was then examined. As shown in Fig. 4B, TiF NPs + US treatment could induce the highest MDA level, which was compatible with the results of LPO expression. It seems that TiF NPs +

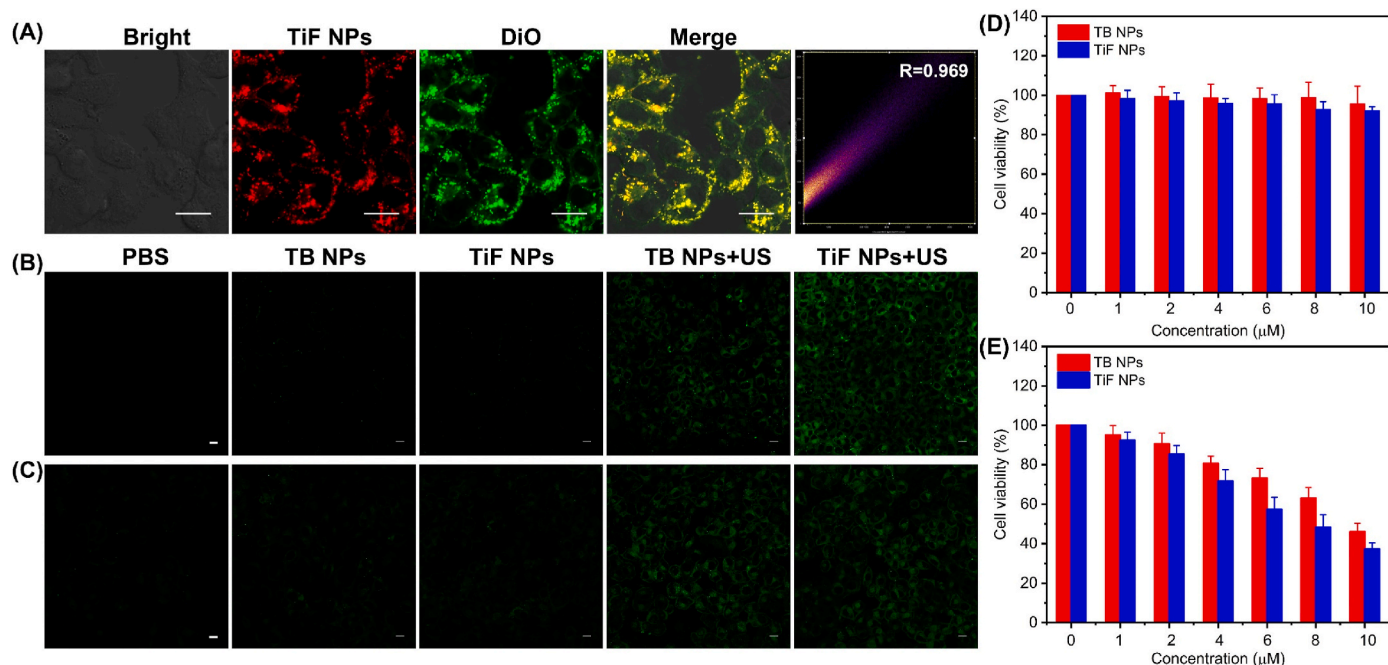


**Fig. 3.** (A) Colocalization of TiF NPs (in red) with DiO (in green) in 4T1 cells, scale bar = 10 μM. (B) ROS detection in 4T1 cells using DCFH-DA as total ROS indicators, scale bar = 10 μM. (C) ROS detection in 4T1 cells using SOSG as  $^1\text{O}_2$  fluorescence indicators, scale bar = 10 μM. (D) The cell viability of 4T1 co-incubated with TiF NPs or TB NPs without US irradiation. (E) The cell viability of 4T1 co-incubated with TiF NPs or TB NPs under US irradiation.

US could accumulate LPO to a high level, which may drive ferroptosis.

Studies have indicated that the FSP1/CoQ10/NADPH axis is an antioxidant approach to suppress ferroptosis. FSP1 acts as an oxidoreductase to facilitate the detoxifying of LPO by coenzyme Q10 (CoQ10) [50,51]. Hence, suppression of FSP1 may drive the accumulation of CoQ10 and reduce nicotinamide adenine dinucleotide phosphate (NADH). Defective detoxifying or over-production of LPO could induce or boost lipid peroxidation to induce ferroptosis [26,52]. We investigated the expression of FSP1, CoQ10, and NADH following various treatments. As observed in Fig. 4C and D, intracellular NADH level was markedly reduced and the  $\text{NAD}^+/\text{NADH}$  ratio increased in TiF NPs + US-treated 4T1 cells, suggesting NADH depletion and subsequent generation of its metabolic product ( $\text{NAD}^+$ ). The intracellular CoQ10 was assessed. There was a significant decrease in TiF NPs + US-treated 4T1 cells (Fig. 4E), which was consistent with the NADH result. As shown in Fig. 4F, the decreased expression of FSP1 was observed in TiF NPs treatment groups with or without US irradiation. All the above results corporately suggested that cell membrane targeting SDT plus FSP1 inhibition could significantly increase oxidative stress and drive ferroptosis through the cooperation of an over-produced LPO and detoxifying of LPO via the elimination of CoQ10.

Moreover, cell membrane targeting SDT could generate ROS *in situ*, which destroys membrane integrity and finally induces cell apoptosis. Plasma membrane damage could up-regulate the expression of proapoptotic protein (Bax) which led to the activation of death protease termed caspase-3 to induce cell apoptosis. The expression of apoptosis-associated proteins such as BAX and caspase 3 were investigated. As shown in Fig. 4F, the expressions of caspase 3 and BAX in TiF NPs + US treated group were significantly higher than those other groups.

SDT induces tumor cell apoptosis and releases DAMPs to activate DCs [53,54]. At the same time, SDT improves the immunogenicity of tumor cells by exposing tumor antigens, resulting in more effective tumor immunotherapy. The three messengers, calreticulin (CRT), high mobility group box B1 (HMGB1), and ATP, function as immunological triggers to further stimulate anti-tumor immune responses [55–57]. Among the treatment groups, the TiF NPs + US group produced the greatest amount of CRT expression on the cell surface (Fig. 4G). Images

showed that the TiF NPs + US group released more HMGB1 from the nucleus than the other group (Fig. 4H). Besides, the released ATP as a “find me” signal exhibited a 4-fold increase in the TiF NPs group, stimulating the specific antitumor immune effect (Fig. 4I). These results were consistent with a significant increase in the HMGB1 release. In the end, it was demonstrated that SDT produced by TiF NPs could successfully induce ICD.

Furthermore, interleukin-6 (IL-6) and tumor necrosis factor- $\alpha$  (TNF $\alpha$ ) release in the ELISA supernatant are additional proinflammatory cytokines. Following TiF NPs + US treatment, greater levels of TNF $\alpha$  and IL-6 secretion were seen as compared to the PBS or TB NPs + US treated groups (Fig. 4K and J). These findings demonstrated that the efficient induction of immunogenic cell death (ICD) caused by simultaneous US treatment of TiF NPs (Fig. 4M).

### 3.5. *In vivo* biosafety and tumor enrichment of TiF NPs

Prior to exploring the antitumoral activity *in vivo*, a systemic toxicity investigation was carried out to prove the biosafety. The biocompatibility of TiF NPs was explored through intravenous injection of TiF NPs into healthy BALB/c mice at the dose of 10 mg/kg, the blood routine test and blood biochemistry were conducted on day 7. The blood biochemistry assay results indicated that hepatic and renal function markers including serum albumin (ALB), alkaline phosphatase (ALP), alanine aminotransferase (ALT), uric acid (UA), blood urea nitrogen (BUN), and creatinine (CR) of the TiF NPs treated mice had no abnormal changes compared with the control group (Fig. S20). Finally, hematoxylin and eosin (H&E) staining of the major organs including heart, liver, spleen, lungs, and kidneys exhibited no histological abnormality, verifying the biocompatibility of TiF NPs (Fig. S21). The results validated that TiF NPs did not cause any obvious side effects.

To further track the TiF NPs *in vivo*, NIR fluorescence imaging was carried out to visualize the distribution of TiF NPs after intravenous injection into mice. As shown in Fig. S22, the NIR fluorescence signal in the tumor areas at 24 h was much higher than other time points. Moreover, *ex vivo* fluorescence imaging confirmed that TiF NPs could accumulate in the tumor tissues and main organs at 24 h post-injection,

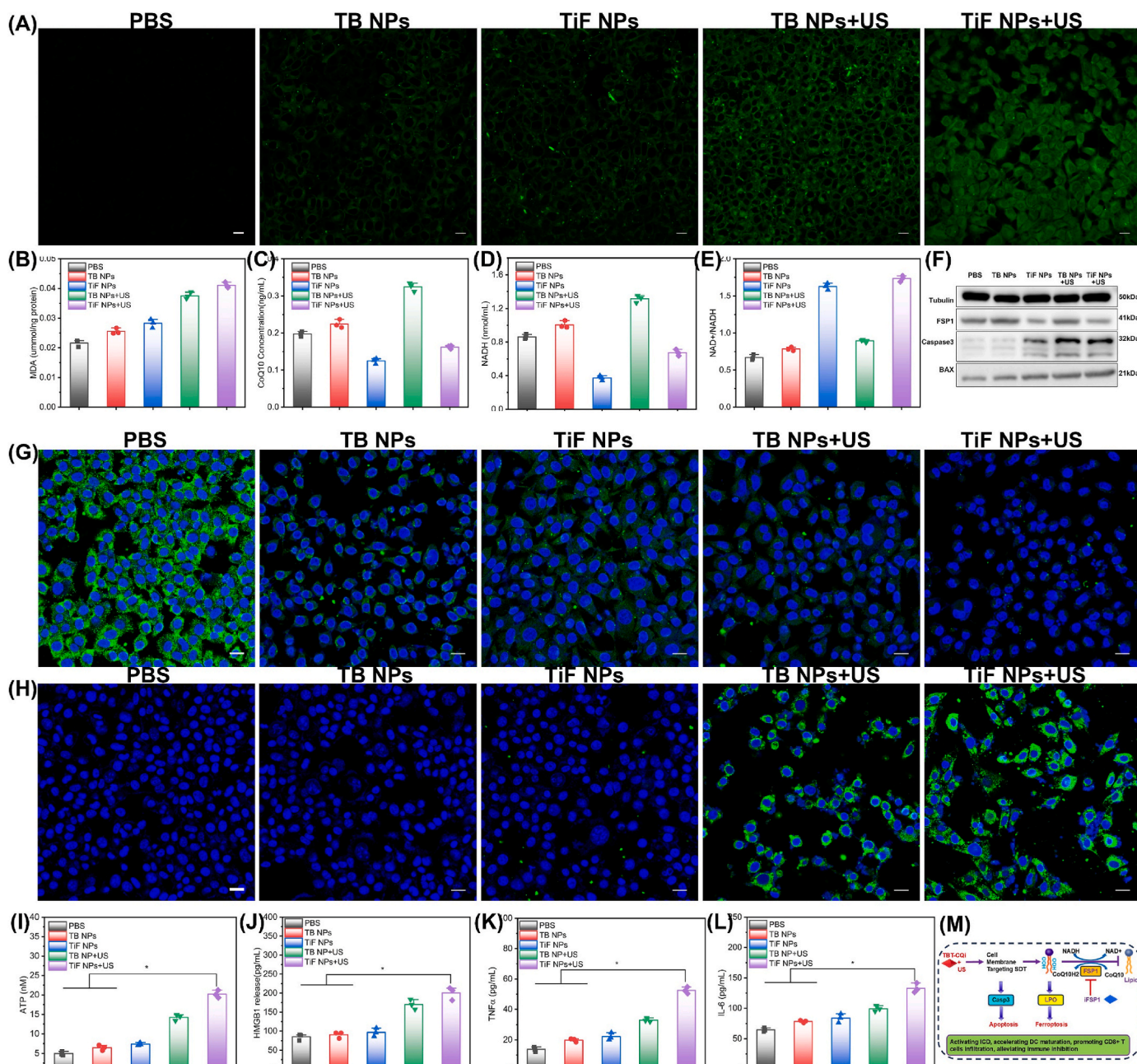


**Fig. 4.** *In vitro* ferroptosis-enhanced SDT effect triggered by TiF NPs. (A) Fluorescent imaging of LPO after various treatments, scale bar = 10 μM. (B) The intercellular MDA level after different treatments. (C) The intercellular NADH level after different treatments. (D) Ratio of intracellular NADP<sup>+</sup>/NADPH after various treatments. (E) The intercellular CoQ10 level after different treatments. (F) Western blotting assay of the FSP1, BAX, Casp3 expression after various treatments. (G) CLSM images of CRT expression in 4T1 cells after various treatments, scale bar = 10 μM. (H) CLSM images of HMGB1 expression in 4T1 cells after various treatments, scale bar = 10 μM. (I) The levels of released ATP in cell culture media after various treatments. (G) The levels of HMGB1 release in cell culture media after various treatments. (K) The levels of TNFα in cell culture media after various treatments. (L) The levels of IL-6 in cell culture media after various treatments. (M) Mechanisms of TiF NPs for cell membrane targeting SDT combination with FSP1 inhibition.

such as the lung and kidney (Fig. S23). Therefore, the 4T1 tumor-bearing mice were treated with US at 24 h after *i.v.* injection of TiF NPs to further evaluate the antitumor and anti-metastasis effect of TiF NPs.

### 3.6. TiF NPs inhibited the tumor growth and lung metastasis

Subcutaneous 4T1 tumor-bearing BALB/c mice were fabricated to investigate the synergistic efficacy of FSP1 inhibition and cell membrane targeting SDT based on TiF NPs *in vivo* (Fig. 5A). The 4T1 tumor-bearing mice were randomly divided into five groups (*n* = 5): (1) PBS group, (2) TB NPs group: *i.v.* injection of TB NPs, (3) TiF NPs group: *i.v.* injection of

TB NPs, (4) TB NPs + US irradiation group: *i.v.* injection of TB NPs and US irradiation, and (5) TiF NPs + US irradiation group: *i.v.* injection of TiF NPs and US irradiation. The ultrasound wave (10 min, 1.0 MHz, 50 % duty cycle, 2.0 W/cm<sup>2</sup>) was performed 24h after intravenous injection. The mice's weight and tumor size were measured every 2 days. Compared with the PBS and TB NPs groups, the TiF NPs group showed a slightly inhibitory effect on tumor growth with a tumor inhibition rate (TIR) of 78.8 %, due to the FSP1 inhibition-induced ferroptosis effects. Furthermore, TB NPs + US showed moderate inhibition on tumor growth with a TIR of 44.2 %, ascribing to the cell-membrane targeting SDT. Moreover, the treatment with TiF NPs + US achieved the highest

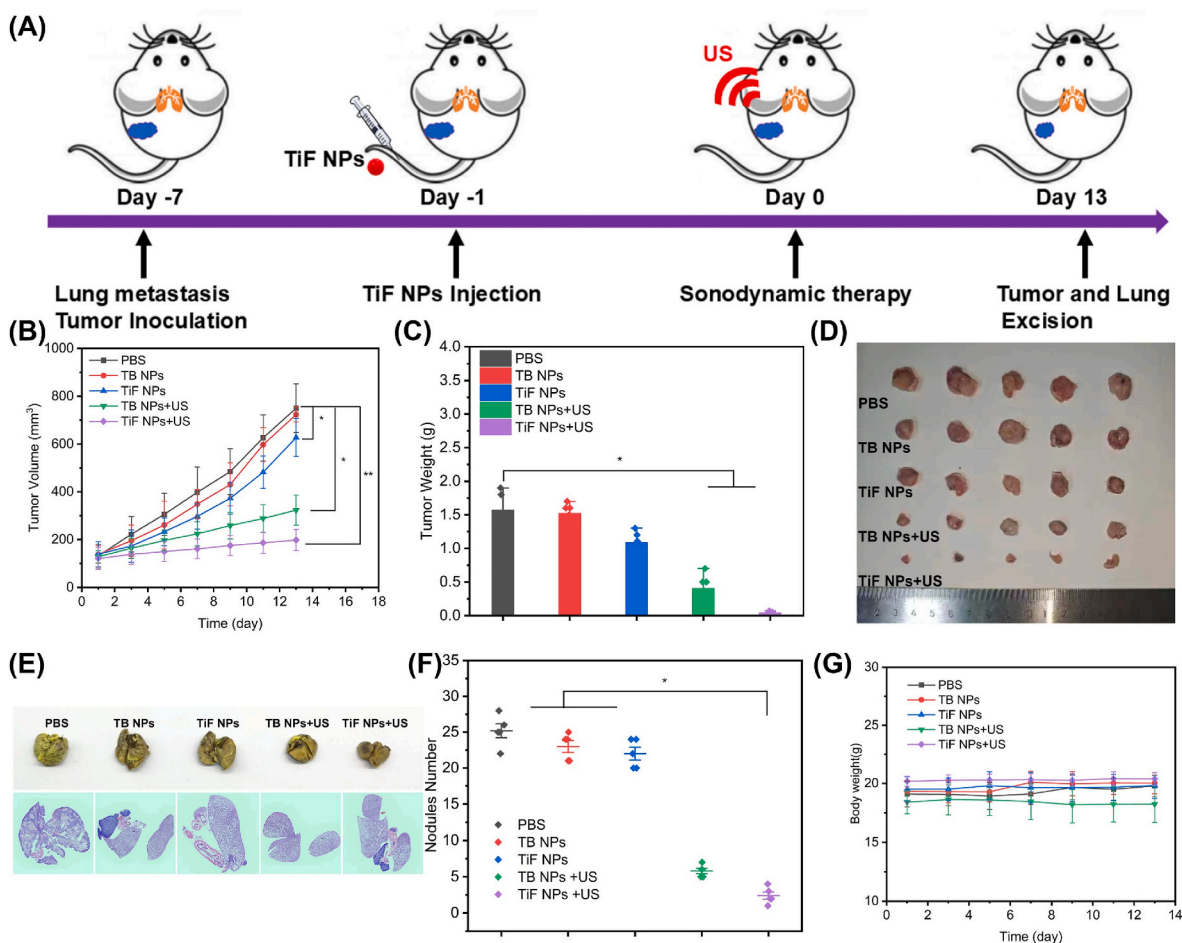


**Fig. 5.** The anti-tumor and anti-metastasis therapeutic evaluation of cell-membrane targeting SDT combination with FSP1 inhibition. (A) Schematic illustration of anti-tumor and anti-metastasis therapy. (B) The tumor growth curving of mice after different treatments. (C) The tumor weight of mice in five groups. (D) The photograph of tumor tissues for five groups. (E) The photos of lungs and H&E staining lung tissues for five groups. (F) The metastasis nodules number in lung tissues in five groups. (G) The body weight of mice in five groups.

TIR of 27.5 % confirming the best antitumor efficacy (Fig. 5B). The variations in the tumor weights (Fig. 5C) in various treatment groups also confirmed that the TiF NPs + US group presented the lowest tumor weight compared with other treatments. The change trend observed by visual comparison was similar to the results of tumor volume and weight, in which the TiF NPs + US significantly inhibited tumor growth *in vivo* (Fig. 5D).

4T1 cells were intravenously injected to induce lung metastasis as a model to investigate the antimetastatic activity of the TiF NPs. Obvious metastasis occurred in the lungs for the PBS, TB NPs, and TiF NPs treated groups, as indicated by the yellow foci in the lungs and as well as the H&E stained lung tissues (Figs. 5E and F, Figs. S24 and S25), whereas the metastasis nodules were reduced by treating with TB NPs and US irradiation, which should be owing to the ICD activation by cell membrane-targeting SDT. In sharp contrast, there were barely visible lung metastatic regions for the TiF NPs + US treated group, which combined functions of both membrane-targeting SDT and FSP1 inhibition-induced ferroptosis, thus achieving the best therapeutic efficiency. In addition, the body weight of mice in each group exhibited no difference, indicating the safety of the *in vivo* application of this system (Fig. 5G). The above results revealed that the TiF NPs + US treatment can inhibit the tumor growth and lung metastasis *in vivo* via the ferroptosis enhanced cell-membrane targeting SDT.

To explore the anti-tumor activity of TiF NPs, the representative tumor tissues were subjected to histological examination using hematoxylin and eosin (H&E) staining and TdT-mediated dUTP nick end

labeling (TUNEL) staining (Figs. S26 and S27). Compared with other treatments, H&E staining showed significant lesions in tumor tissues in TiF NPs + US treatment groups. Moreover, the TiF NPs + US treatment group demonstrated the most apoptotic/necrotic regions, as observed by TUNEL staining. Next, DCFH-DA staining was used to examine the anticancer mechanism of TiF NPs after US radiation (Fig. S28). The DCFH-DA staining results indicated that the TiF NPs + US treatment group had a significantly higher ROS level with green fluorescence than the control groups.

The lipid peroxidation levels of tumor tissues in all groups were also investigated. The results showed that a significantly stronger green fluorescence was observed in the TiF NPs group following US radiation treatment (Fig. S29), indicating that TiF NPs + US treatment group had a significantly higher level of LPO with green fluorescence compared to the control groups.

### 3.7. *In vivo* immune evaluation

The cancer therapy should not only suppress the growth of tumors but also activate systemic immunity to reverse the immunosuppressive microenvironment, thereby inhibiting metastasis. Therefore, the DC maturation, immune cells infiltration, and the proportions of tumor-associated macrophages (TAM) after different treatments were evaluated to elucidate the underlying mechanisms.

The average proportion of mature DCs (CD80<sup>+</sup> CD86<sup>+</sup> DCs) in the TiF NPs + US group substantially increased to ~52.9 %, which is higher



than that in other treatment groups (Fig. 6A), which was quite beneficial for presenting antigens and activating T cells. Therefore, the proportions of CD4<sup>+</sup> and CD8<sup>+</sup> T cells in TiF NPs + US group significantly increased (Fig. 6B), indicating the successful activation of antitumor immune responses. The release of DAMPs by TiF NPs-induced immunogenic cell death promoted antigen presentation and stimulated DC maturation.

Notably, a decrease in myeloid-derived suppressor cells (MDSCs), the immunosuppressive cells, was also detected due to the cell-membrane targeting SDT and ferroptosis triggered by TiF NPs (Fig. 6C). In the TiF NPs + US group, the proportions of anti-inflammatory M2 macrophages decreased, while the number of pro-inflammatory M1 macrophages significantly increased (Fig. 6D and Fig. S30), indicating that cell-membrane targeting SDT and ferroptosis reversed the polarization of TAMs from the anti-inflammatory M2 phenotype to the pro-inflammatory M1 phenotype. All these results confirmed that TiF NPs + US could reverse the immunosuppressive microenvironment.

Finally, the serum levels of immune-relevant inflammatory cytokines, including TNF $\alpha$ , IL-6, and IFN- $\gamma$  were detected (Fig. 6E-G). Compared with those in the other groups, the level of these cytokines significantly increased in the TiF NPs group, verifying the activation of systemic antitumor immune response. Above all, TiF NPs-mediated cell-membrane targeting SDT and ferroptosis efficiently facilitated the infiltration of immune cells, and reversed the immune-suppressive tumor microenvironment, triggering great interest in the treatment of more aggressive and metastatic tumors.

#### 4. Conclusion

In conclusion, we constructed US-active nanoparticles (TiF NPs) to simultaneously deliver organic small sonosensitizer TBT-CQi and iFSP1 to tumor cells for cell membrane-targeting SDT and ferroptosis. On the one hand, the well-designed sonosensitizer TBT-CQi could accumulate in the cell membrane, and intensively disrupt the cell membrane with *in situ* generation of ROS for a highly efficient SDT. More importantly, this membrane-targeting SDT modality could eminently induce LPO and evoke apoptosis. Moreover, iFSP1 could efficiently down-regulate the FSP1-CoQ10-NADH axis, inhibit the expression of FSP1, decrease CoQ10 and NADH, and enhance the LPO level, which evokes ferroptosis for the amplified ICD effect. The cell membrane targeting SDT/FSP1 inhibition triggered ferroptosis was certified to boost systemic antitumor immunity to inhibit the growth of tumors and suppress tumor metastasis. This study represents an effective paradigm for achieving cell membrane-targeting SDT and initiating tumor-specific ferroptosis. Overall, our study provides an inspirational strategy to pursue oncolytic ferroptosis and convert tumor into *in situ* vaccine factories for boosted antitumor immunity.

#### CRediT authorship contribution statement

**Jian Chen:** Validation, Investigation, Formal analysis. **Qiyu Zhan:** Visualization, Software, Methodology, Data curation, Conceptualization. **Lie Li:** Investigation, Data curation. **Simin Xi:** Methodology, Investigation, Data curation. **Longmei Cai:** Methodology, Conceptualization. **Ruiyuan Liu:** Writing – review & editing, Writing – original

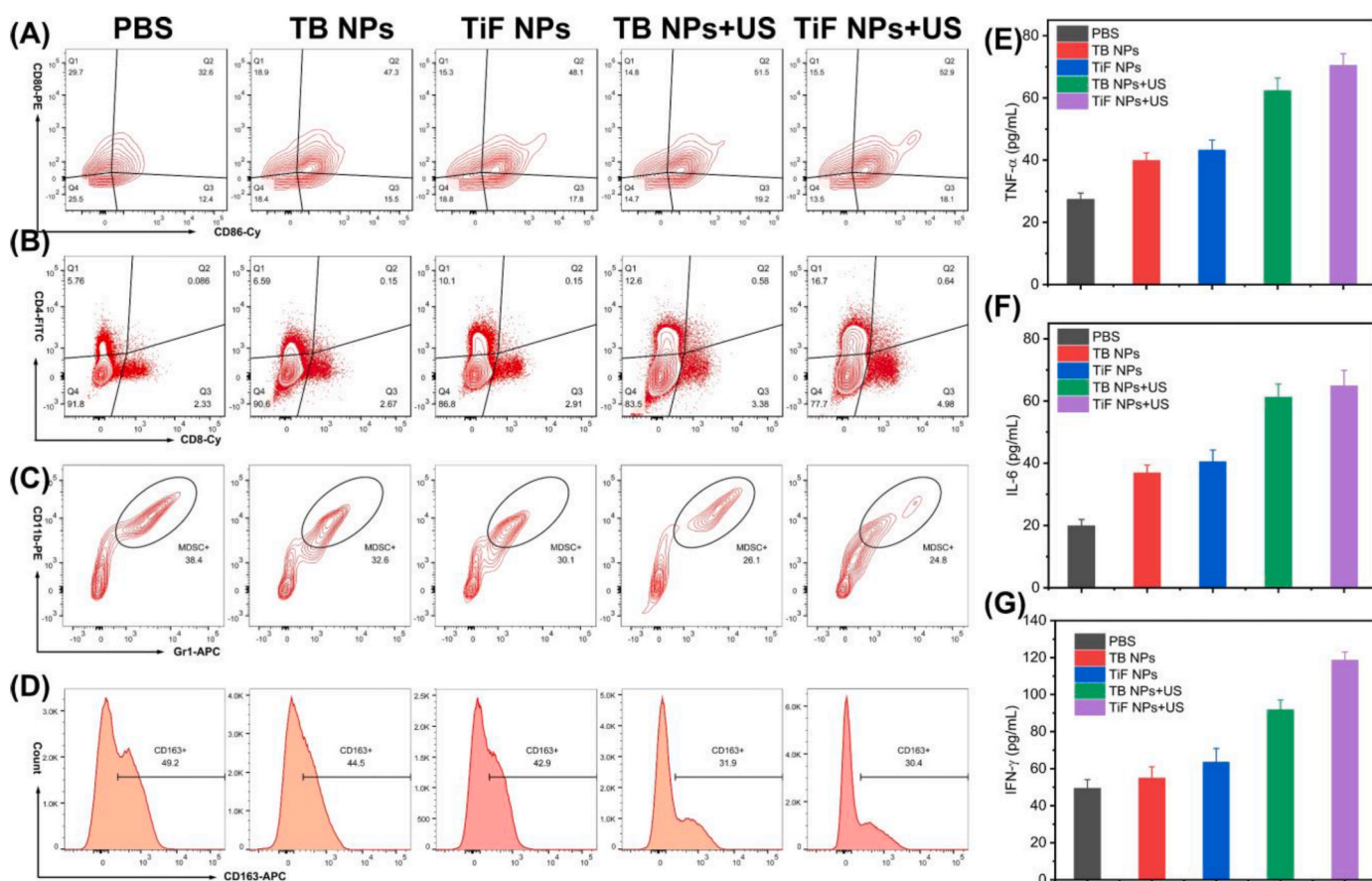


**Fig. 6.** *In vivo* immune responses induced by TiF NPs based cell membrane-targeting type I/II PDT combination with FSP1 inhibition. (A) DC maturation markers (CD80<sup>+</sup> CD86<sup>+</sup>) in the lymph nodes were detected through flow cytometry. (B) CD8<sup>+</sup> T cell proportions among tumor-infiltrating CD3<sup>+</sup> CD45<sup>+</sup> T cells. (C) The proportions of Gr-1+CD11b+ cells among tumor-infiltrating CD45<sup>+</sup> cells. (D) M2-like phenotype macrophages (CD163<sup>+</sup> cells). (E) ELISA detection of the TNF $\alpha$  in tumors. (F) ELISA detection of the IL-6 in tumors. (G) ELISA detection of the IFN- $\gamma$  in tumors.

draft, Methodology, Funding acquisition. **Lujia Chen:** Writing – review & editing, Methodology, Conceptualization.

### Declaration of competing interest

The authors declare the following financial interests/personal relationships which may be considered as potential competing interests: Ruiyuan Liu reports financial support was provided by Southern Medical University. If there are other authors, they declare that they have no known competing financial interests or personal relationships that could have appeared to influence the work reported in this paper.

### Acknowledgements

We gratefully acknowledge financial support from the Natural Science Foundation of Guangdong Province, China (No. 2023A1515012934) and Guangdong Province Marine Economic Development Project (GDNRC[2024]27).

### Appendix A. Supplementary data

Supplementary data to this article can be found online at <https://doi.org/10.1016/j.mtbio.2024.101407>.

### Data availability

The data that has been used is confidential.

### References

- X. Song, Q. Zhang, M. Chang, L. Ding, H. Huang, W. Feng, T. Xu, Y. Chen, Nanomedicine-enabled Sonomechanical, Sonopiezoelectric, sonodynamic, and Sonothermal therapy, *Adv. Mater.* 35 (31) (2023) e2212259.
- Y. Yang, J. Huang, M. Liu, Y. Qiu, Q. Chen, T. Zhao, Z. Xiao, Y. Yang, Y. Jiang, Q. Huang, K. Ai, Emerging sonodynamic therapy-based Nanomedicines for cancer immunotherapy, *Adv. Sci.* 10 (2) (2023) e2204365.
- S. Son, J.H. Kim, X. Wang, C. Zhang, S.A. Yoon, J. Shin, A. Sharma, M.H. Lee, L. Cheng, J. Wu, J.S. Kim, Multifunctional sonosensitizers in sonodynamic cancer therapy, *Chem. Soc. Rev.* 49 (11) (2020) 3244–3261.
- X. Xing, S. Zhao, T. Xu, L. Huang, Y. Zhang, M. Lan, C. Lin, X. Zheng, P. Wang, Advances and perspectives in organic sonosensitizers for sonodynamic therapy, *Coord. Chem. Rev.* 445 (2021) 214087.
- A. Maleki, M. Seyedhamzeh, M. Yuan, T. Agarwal, I. Sharifi, A. Mohammadi, P. Kelicen-Uğur, M. Hamidi, M. Malaki, A.A. Al Kheraif, Z. Cheng, J. Lin, Titanium-based Nanoarchitectures for sonodynamic therapy-Involved Multimodal treatments, *Small* 19 (12) (2023) e2206253.
- Y. Yang, N. Wang, F. Yan, Z. Shi, S. Feng, Metal–organic frameworks as candidates for tumor sonodynamic therapy: Designable structures for targeted multifunctional transformation, *Acta Biomater.* 181 (2024) 67–97.
- P. Yan, L.-H. Liu, P. Wang, Sonodynamic therapy (SDT) for cancer treatment: Advanced Sensitizers by ultrasound activation to Injury tumor, *ACS Appl. Bio Mater.* 3 (6) (2020) 3456–3475.
- S. Liang, X. Deng, P.a. Ma, Z. Cheng, J. Lin, Recent Advances in Nanomaterial-Assisted combinational sonodynamic cancer therapy, *Adv. Mater.* 32 (47) (2020) 2003214.
- X. Pan, H. Wang, S. Wang, X. Sun, L. Wang, W. Wang, H. Shen, H. Liu, Sonodynamic therapy (SDT): a novel strategy for cancer nanotheranostics, *Sci. China Life Sci.* 61 (4) (2018) 415–426.
- L. Pan, J. Liu, J. Shi, Intranuclear photosensitizer Delivery and Photosensitization for enhanced photodynamic therapy with Ultralow irradiance, *Adv. Funct. Mater.* 24 (46) (2014) 7318–7327.
- S.H. Lim, C. Thivierge, P. Nowak-Sliwinka, J. Han, H. van den Bergh, G. Wagnières, K. Burgess, H.B. Lee, In vitro and in vivo photocytotoxicity of boron dipyrromethene derivatives for photodynamic therapy, *J. Med. Chem.* 53 (7) (2010) 2865–2874.
- S. Bai, Z. Lu, Y. Jiang, X. Shi, D. Xu, Y. Shi, G. Lin, C. Liu, Y. Zhang, G. Liu, Nanotransferrin-based programmable Catalysis Mediates three-Pronged induction of oxidative stress to enhance cancer immunotherapy, *ACS Nano* 16 (1) (2022) 997–1012.
- W. Wu, M. Xu, B. Qiao, T. Huang, H. Guo, N. Zhang, L. Zhou, M. Li, Y. Tan, M. Zhang, X. Xie, X. Shuai, C. Zhang, Nanodroplet-enhanced sonodynamic therapy potentiates immune checkpoint blockade for systemic suppression of triple-negative breast cancer, *Acta Biomater.* 158 (2023) 547–559.
- M. Ding, Y. Zhang, N. Yu, J. Zhou, L. Zhu, X. Wang, J. Li, Augmenting immunogenic cell death and Alleviating myeloid-derived suppressor cells by sono-activatable semiconducting polymer Nanopartners for immunotherapy, *Adv. Mater.* 35 (33) (2023) e2302508.
- J. Lei, W. Zhang, L. Ma, Y. He, H. Liang, X. Zhang, G. Li, X. Feng, L. Tan, C. Yang, Sonodynamic amplification of cGAS-STING activation by cobalt-based nanoagonist against bone and metastatic tumor, *Biomaterials* 302 (2023) 122295.
- Y. Yin, X. Jiang, L. Sun, H. Li, C. Su, Y. Zhang, G. Xu, X. Li, C. Zhao, Y. Chen, H. Xu, K. Zhang, Continuous inertial cavitation evokes massive ROS for reinforcing sonodynamic therapy and immunogenic cell death against breast carcinoma, *Nano Today* 36 (2021) 101009.
- W. Wu, M. Xu, B. Qiao, T. Huang, H. Guo, N. Zhang, L. Zhou, M. Li, Y. Tan, M. Zhang, X. Xie, X. Shuai, C. Zhang, Nanodroplet-enhanced sonodynamic therapy potentiates immune checkpoint blockade for systemic suppression of triple-negative breast cancer, *Acta Biomater.* 158 (2023) 547–559.
- H. Lei, J.H. Kim, S. Son, L. Chen, Z. Pei, Y. Yang, Z. Liu, L. Cheng, J.S. Kim, Immunosonodynamic therapy designed with activatable sonosensitizer and immune stimulant Imiquimod, *ACS Nano* 16 (7) (2022) 10979–10993.
- M. Li, Y. Liu, Y. Zhang, N. Yu, J. Li, Sono-Activatable semiconducting polymer Nanoreshapers Multiply Remodel tumor microenvironment for potent immunotherapy of Orthotopic Pancreatic cancer, *Adv. Sci.* 10 (35) (2023) e2305150.
- M. Xu, J. Yu, C. Zhang, C. Xu, X. Wei, K. Pu, Sonodynamic cytokine Nanocomplexes with specific stimulation towards effector T cell for combination cancer immunotherapy, *Angew Chem. Int. Ed. Engl.* 62 (40) (2023) e202308362.
- Z. Yang, D. Tao, W. Zhong, Z. Liu, L. Feng, M. Chen, Perfluorocarbon loaded fluorinated covalent organic polymers with effective sonosensitization and tumor hypoxia relief enable synergistic sonodynamic-immunotherapy, *Biomaterials* 280 (2022) 121250.
- L. Zuo, W. Nie, S. Yu, W.R. Zhuang, C. Liang, S. Li, D. Shi, G. Wu, X. Sui, Y. Li, H. Y. Xie, Biomimetic Nanovesicle with Mitochondria-synthesized sonosensitizer and Mitophagy inhibition for cancer sono-immunotherapy, *Nano Lett.* 23 (7) (2023) 3005–3013.
- N. Yu, M. Li, Y. Zhang, F. Wang, X. Yu, R. Cai, J. Li, Dual-modulation of immunosuppressive pathways using sono-activatable semiconducting polymer nanofeedbacks for cancer immunotherapy, *Nano Today* 52 (2023) 101944.
- Y. Zhu, P. Gong, J. Wang, J. Cheng, W. Wang, H. Cai, R. Ao, H. Huang, M. Yu, L. Lin, X. Chen, Amplification of lipid peroxidation by regulating cell membrane Unsaturation to enhance Chemodynamic therapy, *Angew Chem. Int. Ed. Engl.* 62 (12) (2023) e202218407.
- M.M. Gaschler, B.R. Stockwell, Lipid peroxidation in cell death, *Biochem. Biophys. Res. Commun.* 482 (3) (2017) 419–425.
- J. Fujii, K.I. Yamada, Defense systems to avoid ferroptosis caused by lipid peroxidation-mediated membrane damage, *Free Radic. Res.* 57 (5) (2023) 353–372.
- L.J. Su, J.H. Zhang, H. Gomez, R. Murugan, X. Hong, D. Xu, F. Jiang, Z.Y. Peng, Reactive oxygen species-induced lipid peroxidation in apoptosis, Autophagy, and ferroptosis, *Oxid. Med. Cell. Longev.* 2019 (2019) 5080843.
- D. Li, Y. Yang, D. Li, J. Pan, C. Chu, G. Liu, Organic sonosensitizers for sonodynamic therapy: from small molecules and nanoparticles toward clinical development, *Small* 17 (42) (2021) 2101976.
- K. Liu, Z. Jiang, F. Zhao, W. Wang, F. Jakle, N. Wang, X. Tang, X. Yin, P. Chen, Triarylboron-doped Acenethiophenes as organic sonosensitizers for highly efficient sonodynamic therapy with low phototoxicity, *Adv. Mater.* 34 (49) (2022) e2206594.
- P.H. Zhao, Y.L. Wu, X.Y. Li, L.L. Feng, L. Zhang, B.Y. Zheng, M.R. Ke, J.D. Huang, Aggregation-enhanced sonodynamic activity of Phthalocyanine-Artesunate Conjugates, *Angew Chem. Int. Ed. Engl.* 61 (5) (2022) e202113506.
- J. Chen, Q. Zhou, W. Cao, Multifunctional porphyrin-based sonosensitizers for sonodynamic therapy, *Adv. Funct. Mater.* 34 (40) (2024) 2405844.
- Y. Zhao, J. Liu, M. He, Q. Dong, L. Zhang, Z. Xu, Y. Kang, P. Xue, Platinum-titania Schottky Junction as Nanosonosensitizer, Glucose Scavenger, and tumor microenvironment-Modulator for promoted cancer treatment, *ACS Nano* (2022).
- Y. Zhou, N. Yang, F. Gong, Y. Wang, X. Yang, Y. Dai, Q. Yu, L. Wang, W. Chen, M. Zhuo, L. Cheng, Oxygen-deficient Tungsten Oxide (WO<sub>x</sub>) Nanobelts with pH-Sensitive Degradation for enhanced sonodynamic therapy of cancer, *ACS Nano* (2022).
- Z. Xiao, Q. Chen, Y. Yang, S. Tu, B. Wang, Y. Qiu, Y. Jiang, Q. Huang, K. Ai, State of the art advancements in sonodynamic therapy (SDT): Metal-Organic frameworks for SDT, *Chem. Eng. J.* 449 (2022) 137889.
- B. Geng, J. Hu, Y. Li, S. Feng, D. Pan, L. Feng, L. Shen, Near-infrared phosphorescent carbon dots for sonodynamic precision tumor therapy, *Nat. Commun.* 13 (1) (2022) 5735.
- J. Li, F. Cao, H.L. Yin, Z.J. Huang, Z.T. Lin, N. Mao, B. Sun, G. Wang, Ferroptosis: past, present and future, *Cell Death Dis.* 11 (2) (2020) 88.
- C. Zhang, X. Liu, S. Jin, Y. Chen, R. Guo, Ferroptosis in cancer therapy: a novel approach to reversing drug resistance, *Mol. Cancer* 21 (1) (2022) 47.
- G. Lei, L. Zhuang, B. Gan, Targeting ferroptosis as a vulnerability in cancer, *Nat. Rev. Cancer* 22 (7) (2022) 381–396.
- X. Chen, R. Kang, G. Kroemer, D. Tang, Broadening horizons: the role of ferroptosis in cancer, *Nat. Rev. Clin. Oncol.* 18 (5) (2021) 280–296.
- X. Jiang, B.R. Stockwell, M. Conrad, Ferroptosis: mechanisms, biology and role in disease, *Nat. Rev. Mol. Cell Biol.* 22 (4) (2021) 266–282.
- E. Dai, W. Zhang, D. Cong, R. Kang, J. Wang, D. Tang, AIFM2 blocks ferroptosis independent of ubiquinol metabolism, *Biochem. Biophys. Res. Commun.* 523 (4) (2020) 966–971.
- K. Bersuker, J.M. Hendricks, Z. Li, L. Magtanong, B. Ford, P.H. Tang, M.A. Roberts, B. Tong, T.J. Maimone, R. Zoncu, M.C. Bassik, D.K. Nomura, S.J. Dixon, J. A. Olzmann, The CoQ oxidoreductase FSP1 acts parallel to GPX4 to inhibit ferroptosis, *Nature* 575 (7784) (2019) 688–692.

- [43] S. Doll, F.P. Freitas, R. Shah, M. Aldrovandi, M.C. da Silva, I. Ingold, A. Goya Grocin, T.N. Xavier da Silva, E. Panzilius, C.H. Scheel, A. Mourão, K. Buday, M. Sato, J. Wanninger, T. Vignane, V. Mohana, M. Rehberg, A. Flatley, A. Schepers, A. Kurz, D. White, M. Sauer, M. Sattler, E.W. Tate, W. Schmitz, A. Schulze, V. O'Donnell, B. Proneth, G.M. Popowicz, D.A. Pratt, J.P.F. Angeli, M. Conrad, FSP1 is a glutathione-independent ferroptosis suppressor, *Nature* 575 (7784) (2019) 693–698.
- [44] J. Chen, Z. Duan, L. Deng, L. Li, Q. Li, J. Qu, X. Li, R. Liu, Cell membrane-targeting type I/II photodynamic therapy combination with FSP1 inhibition for ferroptosis-enhanced photodynamic immunotherapy, *Adv. Healthcare Mater.* 13 (16) (2024) 2304436.
- [45] J.W. Kim, M.J. Kim, T.H. Han, J.Y. Lee, S. Kim, H. Kim, K.J. Oh, W.K. Kim, B. S. Han, K.H. Bae, H.S. Ban, S.H. Bae, S.C. Lee, H. Lee, E.W. Lee, FSP1 confers ferroptosis resistance in KEAP1 mutant non-small cell lung carcinoma in NRF2-dependent and -independent manner, *Cell Death Dis.* 14 (8) (2023) 567.
- [46] M. Yang, M.G. Tsui, J.K.W. Tsang, R.K. Goit, K.M. Yao, K.F. So, W.C. Lam, A.C. Y. Lo, Involvement of FSP1-CoQ(10)-NADH and GSH-GPx-4 pathways in retinal pigment epithelium ferroptosis, *Cell Death Dis.* 13 (5) (2022) 468.
- [47] S.J. Dixon, K.M. Lemberg, M.R. Lamprecht, R. Skouta, E.M. Zaitsev, C.E. Gleason, D.N. Patel, A.J. Bauer, A.M. Cantley, W.S. Yang, B. Morrison 3rd, B.R. Stockwell, Ferroptosis: an iron-dependent form of nonapoptotic cell death, *Cell* 149 (5) (2012) 1060–1072.
- [48] Y. Xie, W. Hou, X. Song, Y. Yu, J. Huang, X. Sun, R. Kang, D. Tang, Ferroptosis: process and function, *Cell Death Differ.* 23 (3) (2016) 369–379.
- [49] W.S. Yang, B.R. Stockwell, Ferroptosis: death by lipid peroxidation, *Trends Cell Biol.* 26 (3) (2016) 165–176.
- [50] J.W. Cheu, D. Lee, Q. Li, C.C. Goh, M.H. Bao, V.W. Yuen, M.S. Zhang, C. Yang, C. Y. Chan, A.P. Tse, G.F. Sit, C.X. Liu, I.O. Ng, C.M. Wong, C.C. Wong, Ferroptosis suppressor protein 1 inhibition promotes tumor ferroptosis and anti-tumor immune responses in liver cancer, *Cell Mol Gastroenterol Hepatol* 16 (1) (2023) 133–159.
- [51] P. Koppula, G. Lei, Y. Zhang, Y. Yan, C. Mao, L. Kondiparthi, J. Shi, X. Liu, A. Horbath, M. Das, W. Li, M.V. Poyurovsky, K. Olszewski, B. Gan, A targetable CoQ-FSP1 axis drives ferroptosis- and radiation-resistance in KEAP1 inactive lung cancers, *Nat. Commun.* 13 (1) (2022) 2206.
- [52] C. Mao, X. Liu, Y. Zhang, G. Lei, Y. Yan, H. Lee, P. Koppula, S. Wu, L. Zhuang, B. Fang, M.V. Poyurovsky, K. Olszewski, B. Gan, DHODH-mediated ferroptosis defence is a targetable vulnerability in cancer, *Nature* 593 (7860) (2021) 586–590.
- [53] X. Guo, P. Tu, L. Zhu, C. Cheng, W. Jiang, C. Du, X. Wang, X. Qiu, Y. Luo, L. Wan, R. Tang, H. Ran, Z. Wang, J. Ren, Nanoenabled tumor Energy metabolism Disorder via sonodynamic therapy for Multidrug resistance reversal and metastasis inhibition, *ACS Appl. Mater. Interfaces* 15 (1) (2023) 309–326.
- [54] W. Tang, J. Wu, L. Wang, K. Wei, Z. Pei, F. Gong, L. Chen, Z. Han, Y. Yang, Y. Dai, X. Cui, L. Cheng, Bioactive Layered double Hydroxides for synergistic sonodynamic/Cuproptosis anticancer therapy with Elicitation of the immune response, *ACS Nano* 18 (15) (2024) 10495–10508.
- [55] J.I.G. Solari, E. Filippi-Chiela, E.S. Pilar, V. Nunes, E.A. Gonzalez, F. Figueiró, C. F. Andrade, F. Klamt, Damage-associated molecular patterns (DAMPs) related to immunogenic cell death are differentially triggered by clinically relevant chemotherapeutics in lung adenocarcinoma cells, *BMC Cancer* 20 (1) (2020) 474.
- [56] J. Fucikova, O. Kepp, L. Kasikova, G. Petroni, T. Yamazaki, P. Liu, L. Zhao, R. Spisek, G. Kroemer, L. Galluzzi, Detection of immunogenic cell death and its relevance for cancer therapy, *Cell Death Dis.* 11 (11) (2020) 1013.
- [57] A. Ahmed, S.W.G. Tait, Targeting immunogenic cell death in cancer, *Mol. Oncol.* 14 (12) (2020) 2994–3006.